

# Short-range quasistatic order and critical spin correlations in $\alpha$ -Ru<sub>1-x</sub>Ir<sub>x</sub>Cl<sub>3</sub>

Seung-Hwan Do,<sup>1</sup> W.-J. Lee,<sup>1</sup> S. Lee,<sup>1</sup> Y. S. Choi,<sup>1</sup> K.-J. Lee,<sup>1</sup> D. I. Gorbunov,<sup>2</sup> J. Wosnitza,<sup>2</sup>  
B. J. Suh,<sup>3</sup> and Kwang-Yong Choi<sup>1,\*</sup>

<sup>1</sup>Department of Physics, Chung-Ang University, Seoul 06974, Republic of Korea

<sup>2</sup>Dresden High Magnetic Field Laboratory (HLD-EMFL), Helmholtz-Zentrum Dresden-Rossendorf, Dresden D-01328, Germany

<sup>3</sup>Department of Physics, The Catholic University of Korea, Bucheon 14662, Republic of Korea



(Received 4 April 2018; published 5 July 2018)

The magnetic ground states of the diluted  $\alpha$ -Ru<sub>1-x</sub>Ir<sub>x</sub>Cl<sub>3</sub> are systematically investigated by magnetization, specific heat, and muon spin rotation measurements. Introduction of moderate spin vacancies leads to a destabilization of the zigzag antiferromagnetic order towards a short-range ordered state. It is remarkable that the  $x = 0.2$  sample located near a quantum critical point shows an extremely short correlation length of the magnitude of magnetic moments  $\zeta_{\text{mag}} \sim 1.2a$  ( $a$  = lattice spacing) and a power-law behavior of the magnetic susceptibility  $\chi(T) \sim T^{-p}$  below 14 K for  $\mu_0 H \parallel ab$  and below 30 K for  $\mu_0 H \parallel c$ . Our work demonstrates that the  $\alpha$ -Ru<sub>1-x</sub>Ir<sub>x</sub>Cl<sub>3</sub> system hosts a short-range, quasistatic order characterized by critical spin correlations.

DOI: 10.1103/PhysRevB.98.014407

## I. INTRODUCTION

The exactly solvable Kitaev spin Hamiltonian on a honeycomb lattice is a paradigmatic model to harbor topological order and fractionalization of quasiparticles [1]. In the Kitaev model,  $J_{\text{eff}} = 1/2$  spins are exchange coupled through bond-dependent Ising interactions ( $\mathcal{H} = K_{\gamma} S_i^{\gamma} S_j^{\gamma}$ ;  $\gamma = x, y, z$ ) on the three distinct links of a honeycomb lattice [2]. In close analogy to geometrical frustration in triangular, kagome, and pyrochlore lattices, exchange frustration creates the macroscopic degeneracy of a ground state and, thereby, gives rise to topological quantum spin liquids (QSLs) and spin fractionalization into Majonara fermions (MFs) and static  $Z_2$  gauge fluxes [1]. Recently, the Kitaev QSLs and ensuing MFs have been much sought after with a view towards their application to topological quantum computation [3–7].

In the quest for a Kitaev honeycomb magnet, the two-dimensional layered ruthenate  $\alpha$ -RuCl<sub>3</sub> is considered a prime candidate. In this material, the combination of large spin-orbit coupling, Hund's coupling, and electronic correlations in the Ru<sup>3+</sup>(4d<sup>5</sup>) atom leads to a  $J_{\text{eff}} = 1/2$  pseudospin configuration with one hole in the Kramers doublet of the  $t_{2g}$  sublevels [8,9]. The 94° bonding angle of two Ru-Cl-Ru exchange paths forms a near-optimal geometry that maximizes the Kitaev interaction [10–12]. In addition, the use of Ru<sup>3+</sup> instead of Ir<sup>4+</sup> ions avoids direct and longer-exchange interaction owing to weak trigonal distortions from the cubic structure and smaller orbitals of Ru<sup>3+</sup>. Nonetheless, it is almost impossible to nullify residual Heisenberg ( $J$ ) and off-diagonal symmetric ( $\Gamma$ ) exchange interactions, which stabilize zigzag antiferromagnetic (AFM) order below 6.5 K [11–13]. In spite of the long-range magnetic order, however, there are compelling experimental evidences that  $\alpha$ -RuCl<sub>3</sub> is in close proximity to a QSL phase in the  $K$ - $\Gamma$ - $J$  phase diagram [14–22]. This raises the important question of

whether a QSL phase can be attained by melting the zigzag AFM order through perturbations.

Significantly, the zigzag AFM order of  $\alpha$ -RuCl<sub>3</sub> observed at ambient pressure and zero field becomes destabilized to a quantum disordered state under moderate pressure and in-plane magnetic field [13,23,24]. By the same token, introduction of spin vacancies can offer a promising route to promote a dynamic quantum ground state. Theoretical studies of the diluted Kitaev-Heisenberg model show that small spin vacancies turn the zigzag AFM order into a spin-glass state, reflecting a short-range correlated nature of the Kitaev interaction [25–29], which is clearly distinct from a Heisenberg magnet [30]. A recent study of the diluted  $\alpha$ -Ru<sub>1-x</sub>Ir<sub>x</sub>Cl<sub>3</sub> (Ir<sup>3+</sup>;  $J_{\text{eff}} = 0$ ) has drawn a magnetic phase diagram, evidencing the suppression of the zigzag order toward a diluted spin liquid [31]. This motivates us to detail an evolution of ground state and magnetic correlations in the vicinity of quantum critical points.

In this paper, we employ thermodynamic and muon spin rotation ( $\mu$ SR) techniques to investigate magnetic properties of the diluted  $\alpha$ -Ru<sub>1-x</sub>Ir<sub>x</sub>Cl<sub>3</sub>. We find the two critical points linked to ABC- and AB-type zigzag AFM orders at  $x_{c1} = 0.13$  and  $x_{c2} = 0.24$ . In the intermediate regime ( $x_{c1} < x < x_{c2}$ ), our  $\mu$ SR study unveils a short-range correlated quasistatic order coexisting with dynamically fluctuating moments. A power-law dependence of the low- $T$  magnetic susceptibility suggests that the correlated magnetic moments are subject to critical spin dynamics.

## II. EXPERIMENTAL DETAILS

Single crystals of  $\alpha$ -Ru<sub>1-x</sub>Ir<sub>x</sub>Cl<sub>3</sub> ( $0 \leq x \leq 0.33$ ) were grown by a vacuum sublimation method. A stoichiometric mixture of commercial RuCl<sub>3</sub> and IrCl<sub>3</sub> powders (Alfa-Aesar) were thoroughly ground and dehydrated in a quartz ampoule for two days. The ampoule was sealed in vacuum and placed in a temperature gradient furnace. The temperature of the Ru<sub>1-x</sub>Ir<sub>x</sub>Cl<sub>3</sub> powder is set at 1080 °C. After dwelling for five

\*kchoi@cau.ac.kr

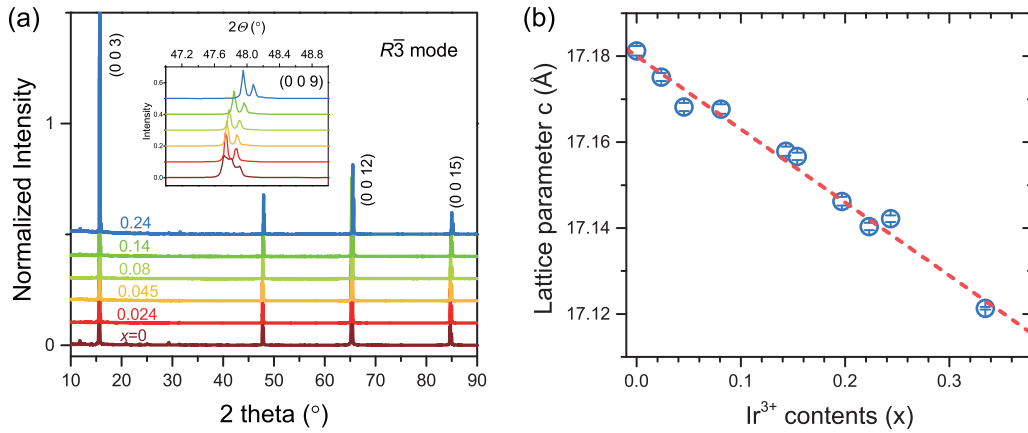


FIG. 1. (a) X-ray diffraction patterns of  $\alpha$ - $\text{Ru}_{1-x}\text{Ir}_x\text{Cl}_3$  ( $0 \leq x \leq 0.33$ ) single crystals at room temperature. Four peaks are indexed with Miller (00l) indices. The inset is a zoom of the (009) peak. The data are vertically shifted for clarity. (b)  $x$  dependence of the  $c$ -axis lattice parameter determined in the rhombohedral ( $R\bar{3}$ ) setting. A red dashed line is a guide to the eye.

hours, the furnace is cooled to 600 °C at a rate of  $-2$  °C/h. The obtained crystals are black with shiny surfaces.

A crystal structure of  $\alpha$ - $\text{Ru}_{1-x}\text{Ir}_x\text{Cl}_3$  was characterized by x-ray powder diffraction (XRD) using Cu  $K\alpha$  radiation (the Bruker D8-advance model). The phase purity and stoichiometry of  $\alpha$ - $\text{Ru}_{1-x}\text{Ir}_x\text{Cl}_3$  were determined by x-ray diffraction and EDX (electron dispersive x ray). The actual compositions of  $\text{Ru}_{1-x}\text{Ir}_x\text{Cl}_3$  used for all experiments were checked using EDX. A variation of the Ru:Ir ratio in a single piece ( $< 2$  mm size) was evaluated by scanning a dozen spots of 50  $\mu\text{m}$  size. Standard deviation from the average value of  $x$  is estimated to be 0.3–2.6 mol% Ir from a Gaussian approximation of the distribution. These values are slightly larger than those reported in Ref. [31]. The small discrepancy is most likely due to the different growth conditions. Notwithstanding, we find no appreciable difference in magnetic properties between the reported and present works (*vide infra*). Here we note that the actual composition  $x$  slightly varies with each experiment because even sample pieces from the same batch have some distribution of compositions.

dc magnetic susceptibility was measured in the temperature range  $T = 2$ –300 K using a commercial SQUID magnetometer (MPMS-5XL SQUID, Quantum Design). An external magnetic field is applied parallel to the plane of platelike crystals ( $\mu_0 H \parallel ab$ ) and perpendicular to the plane ( $\mu_0 H \parallel c$ ). Specific heat was measured at zero magnetic field between 1.8 and 16 K using a heat-pulse relaxation method in a physical properties measurement system (PPMS, Quantum Design). High-field magnetization measurements were performed at the Dresden High Magnetic Field Laboratory using a pulsed-field magnet (25-ms duration) and an induction method with a pickup coil device at  $T = 2.5$  K.

$\mu\text{SR}$  experiments were performed at the M15 and M20 beamlines in TRIUMF (Vancouver, Canada). For the M15 beamline measurements, single crystals were packed in a Ag foil packet and attached to a silver holder by thermal grease. For the M20 beamline measurements, the samples were wrapped in a thin Ag foil packet and glued with Al-mylar tape. Zero- and longitudinal-field  $\mu\text{SR}$  spectra were obtained for temperatures from 1.6 K to 70 K with the LAMPF spectrometer in the M20 beamline and from 30 mK to 4 K with the DR spectrometer in

the M15 beamline. All of the  $\mu\text{SR}$  data were analyzed using the musrfit software package.

### III. RESULTS AND DISCUSSION

#### A. Evolution of lattice parameters

$\alpha$ - $\text{Ru}_{1-x}\text{Ir}_x\text{Cl}_3$  single crystals having a highly two-dimensional layered structure are easily cleaved along the  $ab$  plane. Figure 1(a) shows the XRD patterns of  $\alpha$ - $\text{Ru}_{1-x}\text{Ir}_x\text{Cl}_3$  obtained on the cleaved surface along the (00l) direction at room temperature. The four diffraction peaks are observed in the  $2\theta$  angle range of  $10^\circ \leq 2\theta \leq 90^\circ$  and are indexed to (003), (009), (0012), and (0015) in the  $R\bar{3}$  rhombohedral setting, in which the (006) peak has a very weak intensity. The peak positions are systematically shifted towards higher angles with increasing  $\text{Ir}^{3+}$  content.

The  $c$ -axis lattice parameter was determined by Rietveld Refinements of the XRD patterns using FullProf with preferred oriented crystal modes of  $R\bar{3}$ . The results are plotted in Fig. 1(b). We identify a linear decrease of the  $c$ -axis lattice constant with  $x$ , which agrees well with the earlier report [31]. The quasilinear decrease of the lattice parameter corroborates the structure and the phase purity of the Ir-substituted crystals.

#### B. dc magnetic susceptibility

Figure 2(a) exhibits the temperature dependence of the magnetic susceptibility,  $\chi_{ab}(T)$ , of  $\alpha$ - $\text{Ru}_{1-x}\text{Ir}_x\text{Cl}_3$  ( $0 \leq x \leq 0.25$ ) measured in an applied field of  $\mu_0 H = 0.1$  T for  $\mu_0 H \parallel ab$ . For temperatures below  $T = 150$  K,  $\chi_{ab}(T)$  follows a Curie-Weiss law  $\chi(T) = C/(T - \Theta_{\text{CW}}) + \chi_0$ , as seen from the linear  $T$  dependence of  $1/\chi_{ab}(T)$  in the inset of Fig. 2(a). Here  $C$  is the Curie constant,  $\Theta_{\text{CW}}$  is the Curie-Weiss temperature, and  $\chi_0$  represents the temperature-independent part of the magnetic susceptibility. On introducing nonmagnetic impurities of  $\text{Ir}^{3+}$  to  $\alpha$ - $\text{RuCl}_3$ ,  $\chi_{ab}(T)$  is systematically suppressed and the cusp position in  $\chi_{ab}(T)$  gradually shifts to lower temperature. This shift is clearly visible from the discontinuous jump in the derivative  $d(\chi_{ab})/dT$  [see the vertical arrows in Fig. 2(b)], corresponding to the transition temperature  $T_N$ . With increasing

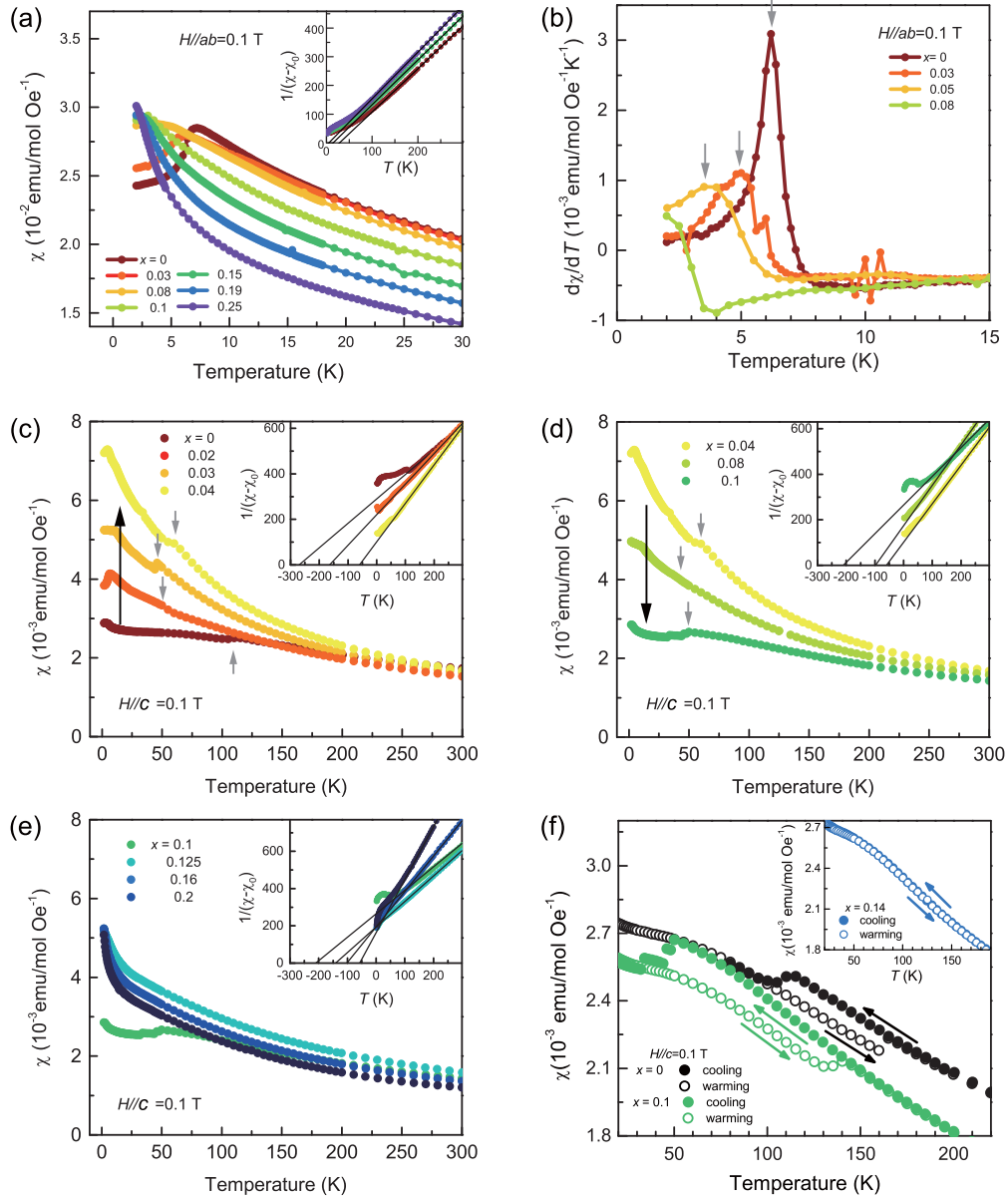


FIG. 2. (a) Temperature-dependent magnetic susceptibility  $\chi(T)$  of  $\alpha$ -Ru<sub>1-x</sub>Ir<sub>x</sub>Cl<sub>3</sub> measured at  $\mu_0 H = 0.1$  T for  $\mu_0 H \parallel ab$ . The inset plots the respective inverse magnetic susceptibility versus temperature. The black solid lines are fits of a Curie-Weiss law to the data. (b) Temperature dependence of the derivative of  $\chi(T)$  with respect to temperature. The peaks in the derivative curves (marked with arrows) correspond to the transition temperatures  $T_N$ . (c)–(e)  $\chi(T)$  of  $\alpha$ -Ru<sub>1-x</sub>Ir<sub>x</sub>Cl<sub>3</sub> measured on cooling at  $\mu_0 H = 0.1$  T for  $\mu_0 H \parallel c$ . For clarity,  $\chi_c(T)$  is separately presented in the three different  $x$  ranges. The insets plot  $1/\chi_c(T)$  versus temperature. The overlaid black lines are fits of Curie-Weiss law to the data. (f) Comparison of the hysteretic behavior of  $\chi_c(T)$  between the parent and  $x = 0.1$  compounds. The inset demonstrates a lacking thermal hysteresis of  $\chi_c(T)$  in the  $x = 0.14$  sample.

Ir content, the transition temperature  $T_N$  gradually decreases [see also the specific heat in Fig. 5(b)].

We now turn to the  $x$  and  $T$  dependence of  $\chi_c(T)$  measured for the field perpendicular to the honeycomb plane ( $\mu_0 H \parallel c$ ). As shown in Figs. 2(c)–2(f),  $\chi_c(T)$  exhibits a distinct jump and pronounced hysteresis in the warming and cooling process up to  $x \sim 0.1$ . This is taken as evidence for the first-order structural phase transition from a high- $T$   $C2/m$  to a low- $T$   $R\bar{3}$  structure. From the fact that the high- $T$  anomaly is observed only in  $\chi_c(T)$ , we infer that the interlayer interactions are largely affected by the structural transition while the intralayer

interactions remain intact. Given that substantial stacking disorders prevent us from observing the structure related anomaly in  $\chi(T)$ , the pronounced anomaly seen in  $\chi_c(T)$  advocates a high quality of our Ir-substituted crystals. However, we find that the structural phase transition temperature does not display a monotonic decrease with increasing  $x$ , as indicated by the down gray arrows. This may be associated with the fact that the crystals from the same batch contain sample pieces with a different degree of the stacking faults.

Figure 2(f) compares the hysteretic loop of  $\chi_c(T)$  between the  $x = 0$  and  $x = 0.1$  samples. Compared to the parent

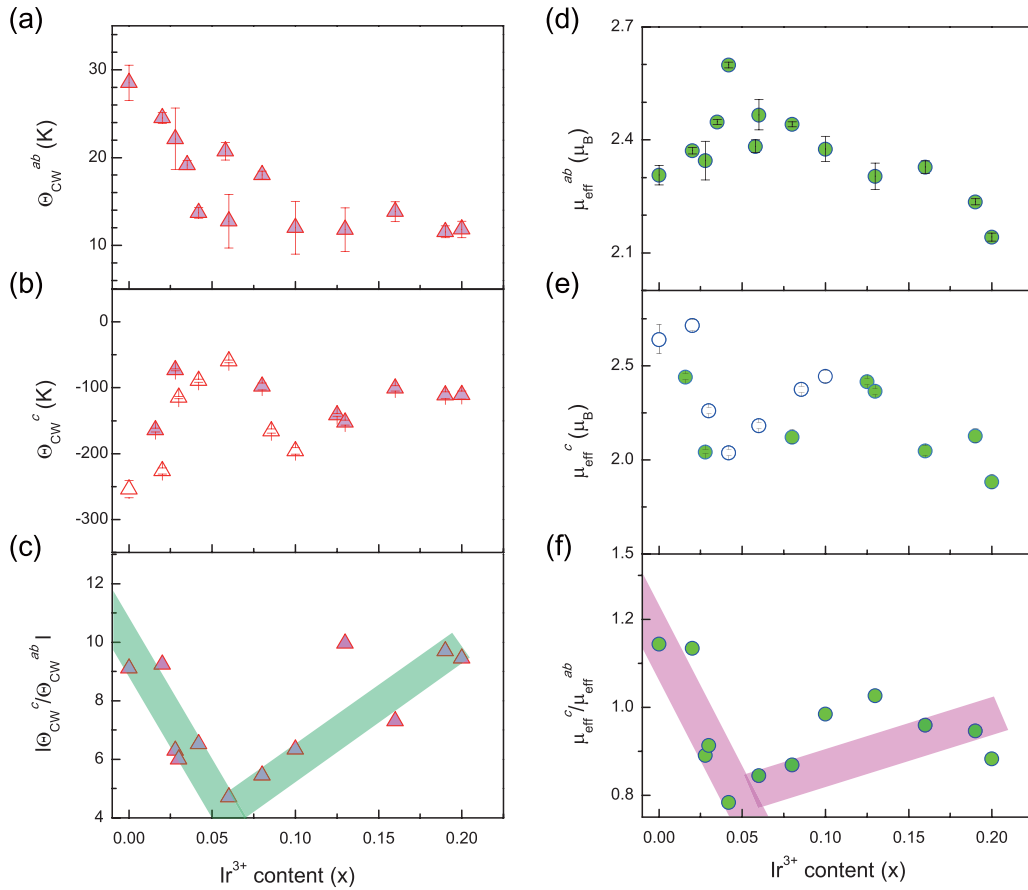


FIG. 3.  $x$  dependence of the Curie-Weiss temperature  $\Theta_{CW}$  for (a)  $\mu_0 H \parallel ab$  and (b)  $\mu_0 H \parallel c$ .  $x$  dependence of the effective magnetic moment  $\mu_{eff}$  for (d)  $\mu_0 H \parallel ab$  and (e)  $\mu_0 H \parallel c$ .  $x$  dependence of (c) the magnetic anisotropies  $|\Theta_{CW}^c(x)/\Theta_{CW}^{ab}(x)|$  and (f)  $\mu_{eff}^c(x)/\mu_{eff}^{ab}(x)$ . The shaded regions are a guide to the eye.

compound, the  $x = 0.1$  sample displays a wider hysteretic loop than the pristine compound, while its structural phase transition temperature is reduced down to  $T_S \sim 50$  K on the cooling cycle. This means that the Ir substitution leads to the proliferation of the AB-type stacking, thereby stabilizing the monoclinic structure against the rhombohedral one. As shown in the inset of Fig. 2(f), the structural phase transition becomes hardly discernible above  $x \sim 0.1$  since a majority of the ABC-type stacking layers turn into the AB-type ones above this substitution level.

We next take a closer look at the  $x$  dependence of  $\chi_c(T)$ . With increasing  $x$ ,  $\chi_c(T)$  first increases steeply up to  $x \sim 0.04$  and then decreases in the range of  $x = 0.04$ – $0.1$ , and finally increases again above  $x > 0.1$  [see Figs. 2(c)–2(e)]. The enhanced  $\chi_c(T)$  at  $x = 0.05$ – $0.06$  leads to a reduced magnetic anisotropy. This anomaly is not an experimental artifact as the magnetization curves display a similar trend as shown in Fig. 4. Rather, this suggests that the  $\text{Ir}^{3+}$  substitution exerts a disparate, nonmonotonic impact on the Kitaev  $K$ , Heisenberg  $J$ , and off-diagonal symmetric exchange interactions  $\Gamma$  as a function of  $x$ .

For a quantitative analysis of the magnetic parameters,  $\chi(T)$  of  $\alpha\text{-Ru}_{1-x}\text{Ir}_x\text{Cl}_3$  is fitted to the Curie-Weiss formula in the temperature range of  $T = 150$ – $300$  K for both field directions. The resulting Curie-Weiss temperatures ( $\Theta_{CW}$ ) and effective magnetic moments ( $\mu_{eff}$ ) are plotted as a function of  $x$  in

Figs. 3(a)–3(b) and Figs. 3(d)–3(e), respectively. For  $\mu_0 H \parallel ab$ , the Curie-Weiss temperature  $\Theta_{CW}^{ab}$  shows a rapid decrease up to  $x \sim 0.1$  and then becomes almost independent of  $x$  above  $x \sim 0.1$ .  $\mu_{eff}^{ab}$  first increases from  $2.3 \mu_B$  at  $x = 0$  to  $2.6 \mu_B$  at  $x = 0.06$  and then gradually decreases to  $2.15 \mu_B$  with further increasing  $x$ . The nonmonotonic  $x$  dependence of  $\mu_{eff}$  together with the constant  $\Theta_{CW}^{ab}$  above  $x \sim 0.1$  is not compatible with the linear decrease expected from an increasing magnetic dilution.

Both  $\mu_{eff}^c$  and  $\Theta_{CW}^c$  exhibit the anomalous  $x$  dependence as well. With increasing  $x$ ,  $\mu_{eff}^c$  and  $|\Theta_{CW}^c|$  decrease steeply up to  $x \sim 0.05$  and then increase in the range of  $x = 0.05$ – $0.1$ , forming a local minimum at about  $x = 0.05$ . Above  $x > 0.1$ , both quantities slowly decrease. We stress that the nonmonotonic evolution of  $\mu_{eff}^c$  and  $\Theta_{CW}^c$  is not consistent with the theoretical prediction of the  $J$ - $K$  model with zigzag AFM order as well as the experimental results of the diluted  $\text{A}_2\text{IrO}_3$  ( $\text{A}=\text{Na}, \text{Li}$ ) iridates [28,30]; the  $J$ - $K$  dominant  $\text{Na}_2\text{IrO}_3$  shows a gradual decrease of  $\mu_{eff}$  and  $\Theta_{CW}$  all the way to a percolation limit while the longer-range  $J$  dominant  $\text{Li}_2\text{IrO}_3$  exhibits no appreciable change of  $\Theta_{CW}$  up to  $x \sim 0.5$ .

To exclude the possibility that the nonmonotonic  $x$  dependence of  $\mu_{eff}$  and  $\Theta_{CW}$  is due to structural imperfections, we selected the data showing only a single magnetic transition. Furthermore, the Curie-Weiss fitting was limited to a high-temperature region above 150 K and was made on the data



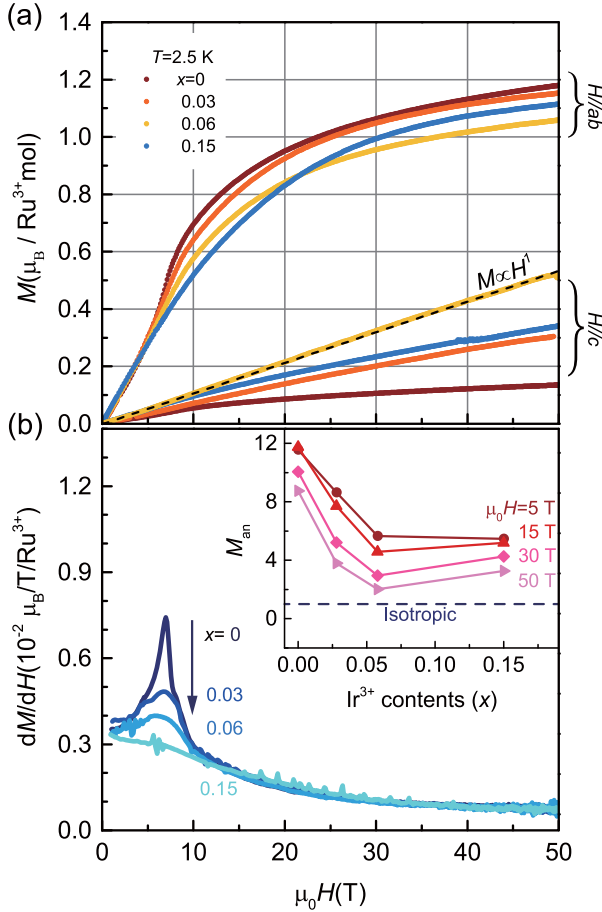


FIG. 4. (a) High-field magnetization curves of  $\alpha$ - $\text{Ru}_{1-x}\text{Ir}_x\text{Cl}_3$  ( $x = 0, 0.03, 0.06$ , and  $0.15$ ) measured at  $T = 2.5$  K for both  $\mu_0 H \parallel ab$  and  $\mu_0 H \parallel c$ . The dashed line is a guide to a linear relation,  $M \propto H$ . (b) Derivative of the magnetization vs field,  $dM_c(H)/dH$  as a function of  $x$ . The inset plots the magnetization anisotropy  $M_{\text{an}}(H) = M_{ab}(H)/M_c(H)$ , a ratio of the in-plane to the out-of-plane magnetization.

obtained on a cooling process. For a further crosscheck, we compare  $\mu_{\text{eff}}^c$  and  $\Theta_{\text{CW}}^c$  extracted from the two distinct classes of materials showing the clear (full symbols) and marginal (open symbols) structural phase transitions. There is no essential difference between them, confirming that the nonmonotonic evolution of  $\mu_{\text{eff}}$  and  $\Theta_{\text{CW}}$  with  $x$  is intrinsic to the  $J$ - $K$ - $\Gamma$  honeycomb system.

Next, we proceed to define the magnetic anisotropies  $|\Theta_{\text{CW}}^c(x)/\Theta_{\text{CW}}^{ab}(x)|$  and  $\mu_{\text{eff}}^c(x)/\mu_{\text{eff}}^{ab}(x)$  from the in- and out-of-plane ratios of the magnetic parameters. From Figs. 3(c) and 3(f), it is evident that both  $|\Theta_{\text{CW}}^c(x)/\Theta_{\text{CW}}^{ab}(x)|$  and  $\mu_{\text{eff}}^c(x)/\mu_{\text{eff}}^{ab}(x)$  decrease quasilinearly with increasing  $x$  up to  $0.05$  and then tend to increase above  $x = 0.05$ . The parent compound has the maximum magnetic anisotropy, whereas at a concentration of about 5% Ir the minimum magnetic anisotropy is attained.

### C. High-field magnetization

Figure 4(a) presents the magnetization curves  $M(H)$  of  $\alpha$ - $\text{Ru}_{1-x}\text{Ir}_x\text{Cl}_3$  ( $x = 0, 0.03, 0.06$ , and  $0.15$ ) measured at  $T = 2.5$  K for the  $\mu_0 H \parallel ab$  plane and  $\mu_0 H \parallel c$  axis with pulsed magnetic fields up to 50 T.  $M(H)$  of the parent compound is

strongly anisotropic between the two field orientations. With increasing  $H$ , the in-plane magnetization  $M_{ab}(H)$  increases steeply with a sharp jump around  $\mu_0 H \sim 7$  T, whereas the out-of-plane magnetization  $M_c(H)$  is weakly  $H$  dependent. Here, the sharp step is associated with a spin-flop-like transition expected for the zigzag-AFM system and heralds a crossover to a partially-polarized quantum disordered phase. With increasing  $x$ , the spin-flop-like transition gradually fades out. This trend can be more clearly visible in a derivative  $dM_{ab}/dH$ .

As shown in Fig. 4(b), the peak in  $dM_{ab}/dH$ , representing the spin-flop-like transition, is progressively suppressed with increasing  $x$ , and finally disappears at  $x \sim 0.15$ . The vanishing crossover is linked to the melting of the zigzag-AFM ordering. As for  $M_c(H)$ , the overall magnetization increases rapidly up to  $x \sim 0.06$  and then decreases above  $x > 0.06$ . To quantify this behavior, we define the magnetization anisotropy  $M_{\text{an}}(H) = M_{ab}(H)/M_c(H)$ . As plotted in the inset of Fig. 4(b),  $M_{\text{an}}(H)$  is the smallest at  $x \sim 0.06$ . The essentially same conclusion is drawn from the analysis of  $|\Theta_{\text{CW}}^c(x)/\Theta_{\text{CW}}^{ab}(x)|$  and  $\mu_{\text{eff}}^c(x)/\mu_{\text{eff}}^{ab}(x)$ . It is remarkable that  $M_c(H)$  of the  $x = 0.06$  sample displays a linear field dependence, typical for an AFM system. This cannot be mere coincidence as discussed in Sec. III B. Taken together, our magnetization study of  $\alpha$ - $\text{Ru}_{1-x}\text{Ir}_x\text{Cl}_3$  collectively suggests that the magnetic anisotropy and exchange interactions evolve in an intriguing way through  $x \sim 0.06$ , demanding a future theoretical study on the dilution effect of the  $J$ - $K$ - $\Gamma$  model with different signs of the exchange interactions.

### D. Specific heat and magnetic phase diagram

Figure 5(a) summarizes the phase diagram of  $\alpha$ - $\text{Ru}_{1-x}\text{Ir}_x\text{Cl}_3$  ( $0 \leq x \leq 0.33$ ).  $T_N^{\text{ABC}}$  and  $T_N^{\text{AB}}$  refer to the ABC- and AB-type zigzag AFM order, respectively. We note that the two successive transitions result from the creation of AB stacking faults in the ABC-type stacking matrix by chemical substitution [14,32]. The  $x$  dependence of  $T_N^{\text{ABC}}$  and  $T_N^{\text{AB}}$  was determined from the peak in specific heat, the cusp of magnetic susceptibility, and the onset of the internal static field by zero-field  $\mu\text{SR}$  (see Sec. III E). All estimates coincide well with each other and are consistent with earlier work [31]. Here we note that  $\mu\text{SR}$  (pink stars) probes either the AB-AFM or the ABC-AFM order. This may be linked to the fact that the volume fraction of the AB-AFM ordered phase is minute below  $x_{c1}$ , whereas its volume fraction becomes dominant above  $x_{c1}$ . Thus, the weak internal field stemming from the minor phase could not be resolved.

Shown in Fig. 5(b) is the low- $T$  specific heat  $C_P/T$  of  $\alpha$ - $\text{Ru}_{1-x}\text{Ir}_x\text{Cl}_3$ . The parent compound undergoes a single transition at  $T_N^{\text{ABC}} = 6.5$  K, indicating the formation of the nearly uniform ABC-type stacking. With increasing  $x$ , the primary peak in  $C_P/T$  is progressively suppressed and shifts to zero Kelvin (marked by the arrows). Noteworthy is that the higher- $T$  secondary peak at  $T_N^{\text{AB}}$  becomes visible above  $x \sim 0.05$  and disappears above  $x \sim 0.15$ . This is ascribed to a growing number of AB stacking faults produced by substituting  $\text{Ir}^{3+}$  for  $\text{Ru}^{3+}$ . A linear extrapolation of the transition temperatures allows determining the two putative critical points at  $x_{c1} = 0.13$  for  $T_N^{\text{ABC}}(x)$  and  $x_{c2} = 0.24$  for  $T_N^{\text{AB}}(x)$ . The AB-type stacking phase becomes predominant over the

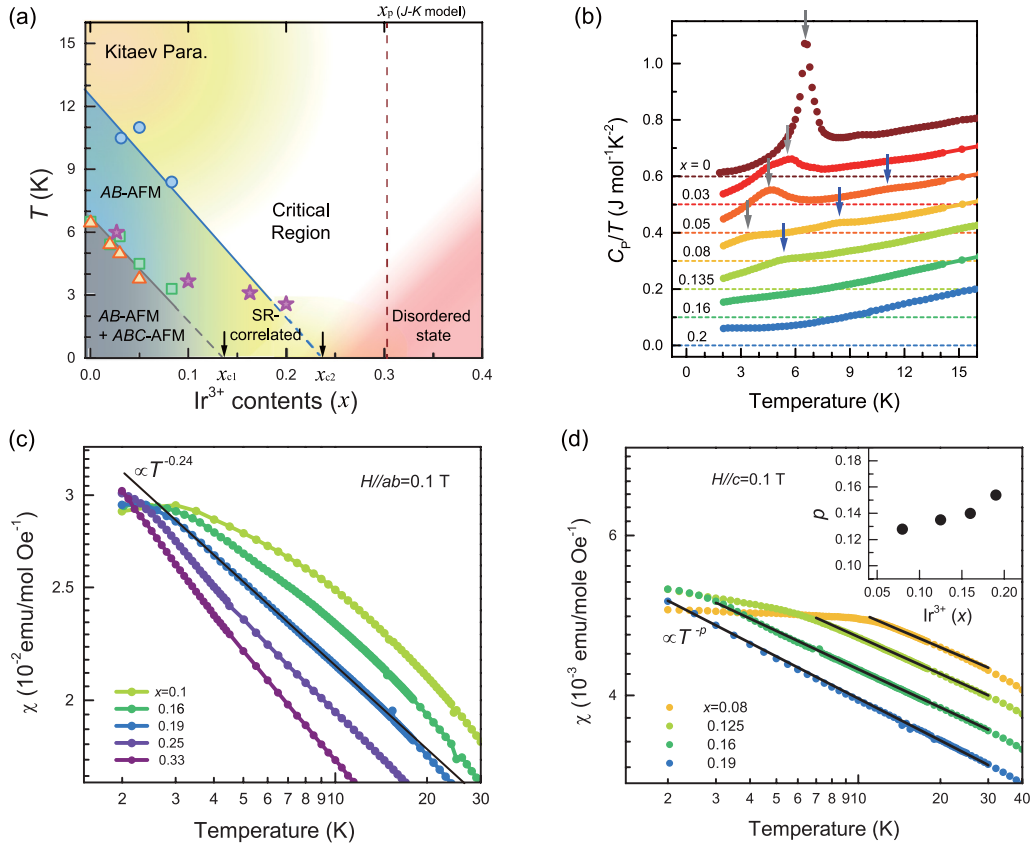


FIG. 5. (a) Magnetic phase diagram of  $\alpha\text{-Ru}_{1-x}\text{Ir}_x\text{Cl}_3$ . Transition temperatures related to the ABC- and AB-type zigzag antiferromagnetic order are determined from magnetic susceptibility (orange triangles), specific heat (green squares and blue circles), and muon spin rotation (pink stars). Linear guide lines represent phase boundaries of AB-AFM (blue shading) and ABC-AFM (gray shading) order, respectively. The linear extrapolations of  $T_N$  to zero temperature are marked with  $x_{c1}$  and  $x_{c2}$ . (b) Low-temperature specific heats of  $\alpha\text{-Ru}_{1-x}\text{Ir}_x\text{Cl}_3$  measured at zero field. The specific heat curves are vertically shifted for clarity. The arrows mark the peaks of the ABC-type (gray) and the AB-type transition temperature (blue). (c),(d) Low-temperature magnetic susceptibility  $\chi(T)$  of  $\alpha\text{-Ru}_{1-x}\text{Ir}_x\text{Cl}_3$  for  $\mu_0 H \parallel ab$  and  $\mu_0 H \parallel c$ , respectively, plotted on a log-log scale. Solid lines indicate a power-law behavior of  $\chi(T) \sim T^{-p}$ . The inset shows the extracted exponent as a function of  $\text{Ir}^{3+}$  content.

ABC-type stacking phase above  $x_{c1}$ . This is fully consistent with the absence of the first-order structural phase transition in the respective  $x$  range [see Fig. 2(d)]. The anticipated critical point at  $x_{c2}$  is close to the percolation limit  $x \sim 0.3$  as known for the Kitaev honeycomb lattice [28,30]. Compared to the ABC-stacking related phase, the longer survival of the AB-stacking phase with dilution may be due to either stronger frustration of interplane interactions or a less predominance of the Kitaev to non-Kitaev terms.

Figures 5(c) and 5(d) zoom in the low- $T$  dependence of the magnetic susceptibility  $\chi(T)$  of  $\alpha\text{-Ru}_{1-x}\text{Ir}_x\text{Cl}_3$ . For  $\mu_0 H \parallel ab$ , a power-law behavior  $\chi(T) \propto T^{-p}$  with  $p = 0.21\text{--}0.24$  is identified in a limited low- $T$  interval as  $x$  approaches  $x_{c2}$ . For  $\mu_0 H \parallel c$ , the power-law dependence with smaller exponent  $p = 0.13\text{--}0.15$  is observed at  $x = 0.08\text{--}0.2$  in a wider range of temperatures up to 30 K. Such a power-law divergence in  $\chi(T)$  is reported for a system near a quantum critical phase transition [33,34], suggesting that  $\alpha\text{-Ru}_{1-x}\text{Ir}_x\text{Cl}_3$  ( $x > x_{c1}$ ) is dominated by critical spin dynamics.

### E. ZF- and LF- $\mu$ SR

With a view to elucidating the ground state of the intermediate phase samples, we performed  $\mu$ SR experiments.

This technique measures the muon spin polarization  $P_z(t)$  as a function of time, which delivers information about the spatiotemporal structure of local magnetic fields in the sample.

The time-dependent  $P_z(t)$  of  $x = 0.03, 0.1, 0.16$  and  $x = 0.2$  in zero external field is shown in Figs. 6(a) and 6(b) at  $T = 30\text{ mK--}10\text{ K}$ . The ZF- $\mu$ SR spectra above 10 K exhibit a very weak depolarization with a Gaussian relaxation form, typical for muon depolarization submitted to a static distribution of random local magnetic fields mainly from nuclear magnetic moments. On cooling towards  $T_N$ , the depolarization increases sharply, pointing to a development of Ru spin correlations. At the base temperature of 30 mK,  $P_z(t)$  displays either a shallow dip or a kink without developing oscillations. In addition, the long-time muon polarization does not reach one third of the initial asymmetry. This demonstrates a development of quasistatic order where the disordered static magnetic moments are short-ranged correlated.

The quasistatic magnetism is well captured by the Gaussian-broadened Gaussian (GbG) depolarization function  $P_{\text{GbG}}(t; \Delta_0, W)$  [35], modeling a broader field distribution than the Gaussian one. The GbG depolarization function is defined as a convolution of the Gaussian Kubo-Toyabe (KT) function

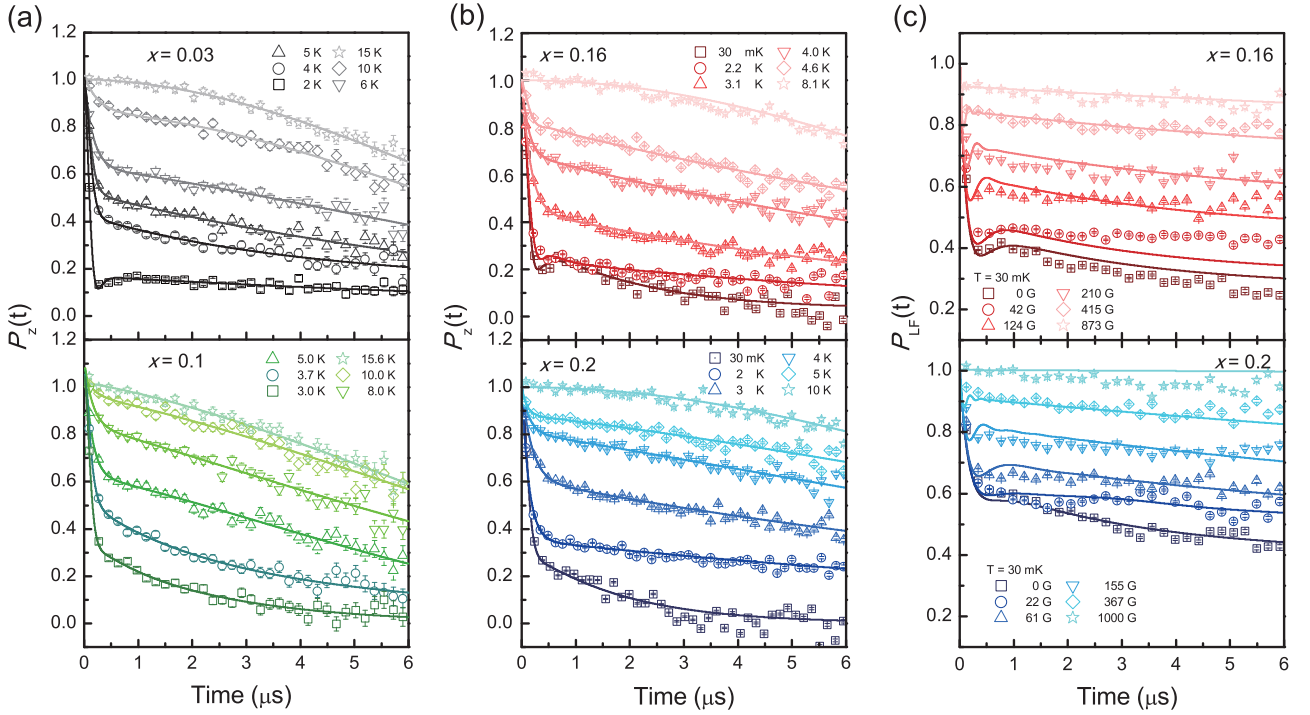


FIG. 6. (a) Temperature dependence of the zero-field muon depolarization  $P_z(t)$  of  $\alpha$ -Ru $_{1-x}$ Ir $_x$ Cl $_3$  ( $x = 0.03$ ) (upper panel) and  $x = 0.1$  (lower panel). (b) Representative  $P_z(t)$  of  $x = 0.16$  (upper panel) and  $x = 0.2$  (lower panel) at selected temperatures. (c) Longitudinal-field dependence of  $P_{LF}(t)$  of  $x = 0.16$  (upper) and  $x = 0.2$  (lower panel) measured at  $T = 30$  mK in a magnetic field  $H = 0$ –1 kG. The solid lines are fits to the data using a sum of the Gaussian broadened Gaussian function  $P_{GbG}(t; \Delta_0, W)$  and a simple exponential function described in the text.

$G_{KT}(\Delta; t)$  with Gaussian field distribution [36]:

$$P_{GbG}(t) = \frac{1}{3} + \frac{2}{3} \left( \frac{1}{1 + R^2 \Delta_0^2 t^2} \right)^{3/2} \left( 1 - \frac{\Delta_0^2 t^2}{1 + R^2 \Delta_0^2 t^2} \right)^{3/2} \times \exp \left( -\frac{\Delta_0^2 t^2}{2(1 + R^2 \Delta_0^2 t^2)} \right). \quad (1)$$

Here  $\Delta_0$  and  $W$  are the mean value and Gaussian width of the Gaussian distribution with the relative width  $R = W/\Delta_0$  [35,36]. This GbG form is known to account for the magnetism in the spin ice magnet Yb $_2$ Ti $_2$ O $_7$  and the hyperkagome antiferromagnet Na $_4$ Ir $_3$ O $_8$ , featuring inhomogeneous static magnetic moments with short-range correlations [36–39].

The experimental spectra were fitted by a sum of the GbG depolarization modified with a simple exponential decay function and a simple exponential component,

$$P_z(t) = f P_{GbG}(t; \Delta_0, W) e^{-\lambda t} + (1 - f) e^{-\lambda_{fast} t}, \quad (2)$$

where  $f$  is the relative amplitude, representing the fraction of quasistatic order in the sample. The second simple exponential term describes dynamically fluctuating moments. The fraction of frozen moments at the base temperature  $T = 30$  mK is given by  $f = 0.74$  (0.5) for the  $x = 0.16$  (0.2) sample. As expected, a dynamic fraction of the sample becomes enhanced with  $x$ . However, no systematic comparison of  $f$  is made for all the studied samples since the measured temperature of the  $x = 0.03$  and 0.1 samples is higher than 2 K.

Several comments on adopting the GbG function are in order. First, it is well established that the magnetism of  $\alpha$ -RuCl $_3$  varies with a stacking pattern and the Ir $^{3+}$  substitution induces

structural inhomogeneities [14,31]. Even a single piece of the sample contains some distribution of the composition  $x$ . Thus, an inhomogeneous distribution of the quasistatic magnetic moments is expected to appear upon introducing spin vacancies. Second,  $G_{KT}(\Delta; t)$  supplemented with a simple exponential is employed to fit the  $\mu$ SR data. Overall the GbG function is found to provide a better description of all the experimental data than the KT function (not shown here).

Further evidence for an inhomogeneous mix of the quasistatic and dynamic magnetism comes from longitudinal-field (LF)  $\mu$ SR measurements where an external field is applied parallel to the initial muon spin direction. As shown in Fig. 6(c), the  $T = 30$  mK  $\mu$ SR spectrum exhibits a systematic shift upward with increasing field. A nearly full polarization of the LF- $\mu$ SR spectra occurs at  $H \approx 1$  kG. From this decoupling field, the local static field is estimated to be  $\langle B \rangle_{loc} \approx 100$  G, corresponding to one tenth of 1 kG (see below for an independent confirmation). Even at high fields of  $H \approx 1$  kG, however, a weakly relaxing component is discernible, confirming the coexistence of the frozen and dynamic fractions of the sample. Fits to the ZF- $\mu$ SR spectra using Eq. (2) yield the  $T$  and  $x$  dependence of the fitting parameters.

In Figs. 7(a)–7(c), we plot the  $T$  dependence of  $\Delta_0$ ,  $R$ , and  $\lambda$  for  $x = 0.16$  and 0.2. With decreasing temperature below  $T_N = 3.1$  K (2.6 K) for  $x = 0.16$  (0.2), the average internal field  $\Delta_0(T)$  shows an order-parameter-like increase described by the phenomenological equation  $\Delta_0(T) \propto (1 - (T/T_N)^\delta)^\beta$ , where  $\beta = 0.110$  (0.127) is for the  $x = 0.16$  (0.2) sample and  $\delta$  is the dimensionality of lattices. The obtained critical exponent is reminiscent of the theoretical value  $\beta = 0.125$  of the

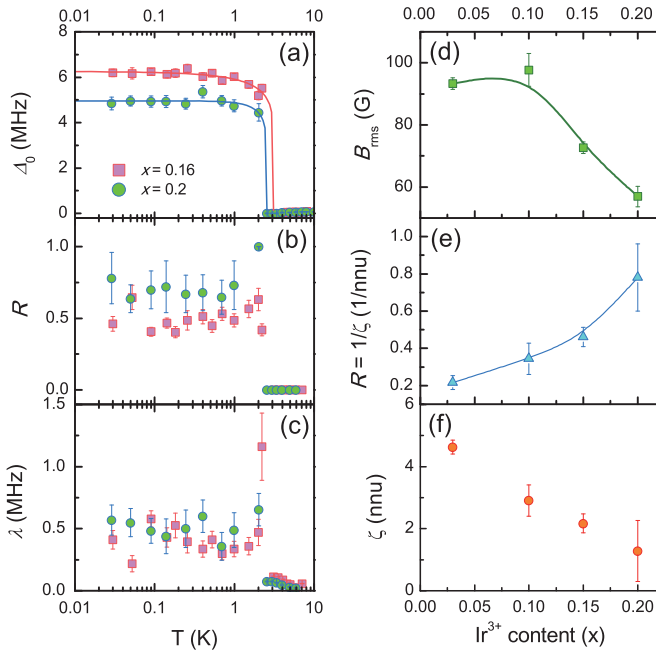


FIG. 7. (a) Temperature dependence of the average of local internal field  $\Delta_0(T)$  for  $x = 0.16$  (pink squares) and  $0.2$  (green circles) on a semilogarithmic scale. The solid lines are fits to the phenomenological function  $\Delta_0(T) \propto (1 - (T/T_N)^\delta)^\beta$ . (b) Temperature dependence of the relative width  $R = 1/\zeta_{\text{mag}}$ . (c) Muon spin relaxation rate vs temperature on a semilogarithmic scale. (d) Local internal field  $\langle B \rangle_{\text{rms}}$  as a function of Ir concentration. (e) Relative width  $R$  as a function of Ir concentration. (f) Magnetic correlation length  $\zeta_{\text{mag}}$  vs  $\text{Ir}^{3+}$  content in the nearest-neighbor unit.

two-dimensional Ising model. Due to a scarcity of data close to  $T_N$ , however, this value should be regarded as a phenomenological parameter. The  $T$  dependence of the relative width  $R(T)$  shows a jump at  $T_N$  and a subsequent leveling off below 1 K. Upon cooling through 10 K, the  $T$  dependence of the ZF muon relaxation rate  $\lambda(T)$  displays a significant increase with a weak peak at  $T_N$  and then becomes  $T$  independent. Along with the weak  $\lambda$ -like peak in  $\lambda(T)$ , the  $T$ -independent behavior of both  $\lambda(T)$  and  $R(T)$  below  $T_N$  indicates persisting magnetic fluctuations in the quasistatic ordered state. The persistent magnetic fluctuations below 1 K are not totally unexpected because the dynamic fraction of the sample behaves like a diluted spin liquid in the percolation limit [31].

Shown in Fig. 7(d) is the  $x$  dependence of the root-mean-square of the internal magnetic field  $\langle B \rangle_{\text{rms}} = \Delta_0/\gamma_\mu$ , where  $2\pi\gamma_\mu = 135.54 \text{ MHz/T}$  is a gyromagnetic ratio of the muon spin. The obtained field is comparable to the local static field of 100 G estimated by the LF- $\mu\text{SR}$  data. Above  $x_{c1}$ ,  $\langle B \rangle_{\text{rms}}$  is strongly reduced to 58 G at  $x = 0.2$ , indicative of

a very weak magnetic order. According to the Monte Carlo simulations on a short-range correlated spin cluster model [35], the relative width  $R$  is inversely proportional to the magnetic correlation length of a moment magnitude,  $\zeta_{\text{mag}}$ . Here we stress that  $\zeta_{\text{mag}}$  is nothing to do with a spin-spin correlation length. Within the GbG model, it represents the correlation length of the magnitude of the ordered magnetic moments. Figures 7(e) and 7(f) present the relative width  $R$  and the magnetic correlation length  $\zeta_{\text{mag}}$  as a function of  $x$ . Introducing spin vacancies drastically reduces the magnetic correlation length from  $\zeta_{\text{mag}} = 7a$  ( $a$ =nearest-neighbor lattice spacing) at  $x = 0.03$  to  $\zeta_{\text{mag}} = (1.2-2)a$  at  $x = 0.16-0.2$ . This observation implies that the intermediate phase of the  $\alpha\text{-Ru}_{1-x}\text{Ir}_x\text{Cl}_3$  system is characterized by an extremely short-ranged quasistatic moment, possibly arising from a strong exchange frustration intrinsic to the Kitaev paramagnet.

#### IV. CONCLUSIONS

In summary, combining magnetization, specific heat, and muon spin rotation techniques, we have drawn the phase diagram of  $\alpha\text{-Ru}_{1-x}\text{Ir}_x\text{Cl}_3$  that maps out the  $x$  dependence of the magnetic phase. We identify the two magnetic transitions linked to ABC- and AB-type zigzag AFM orders. With increasing  $x$ , the ABC-type zigzag AFM order vanishes first at  $x_{c1} = 0.13$  and then the AB-type weak zigzag AFM order disappears at  $x_{c2} = 0.24$ , resulting in the two critical points. At low temperatures of the intermediate regime ( $x_{c1} < x < x_{c2}$ ), our  $\mu\text{SR}$  study reveals a short-range correlated quasistatic order coexisting with dynamically fluctuating moments. A nearly static broader-than-Gaussian field distribution is ascribed to the AB-type stacking faults produced by the chemical substitution. The salient feature of the fluctuating quasistatic state is its extremely short magnetic coherence length of  $\zeta_{\text{mag}} \sim (1.2 - 2)a$ . In this regime, the low- $T$  magnetic susceptibility displays a power-law behavior  $\chi(T) \propto T^{-p}$  with  $p = 0.13-0.15$  for  $\mu_0 H \parallel c$  and with  $p = 0.21-0.24$  for  $\mu_0 H \parallel ab$ , providing evidence for the critical spin correlations. Our results demonstrate that a diluted  $K$ - $\Gamma$ - $J$  ruthenium honeycomb system hosts an unconventional ground state and shows a nonmonotonic evolution of magnetic properties as a function of Ir concentration.

#### ACKNOWLEDGMENTS

We would like to thank B. Hitti for his assistance with the  $\mu\text{SR}$  experiments. This work was supported by Korea Research Foundation (KRF) Grants (No. 2018-0189, No. 2018-0099, and No. 2009-0093817) funded by the Korea government (MEST). We acknowledge the support of the Deutsche Forschungsgemeinschaft (DFG) through SFB 1143 and of the HLD at HZDR, member of the European Magnetic Field Laboratory (EMFL).

- [1] A. Kitaev, Anyons in an exactly solved model and beyond, *Ann. Phys. (NY)* **321**, 2 (2006).
- [2] G. Jackeli and G. Khaliullin, Mott Insulators in the Strong Spin-Orbit Coupling Limit: From Heisenberg to a Quantum Compass and Kitaev Models, *Phys. Rev. Lett.* **102**, 017205 (2009).

- [3] J. Knolle, G. W. Chern, D. L. Kovrizhin, R. Moessner and N. B. Perkins, Raman Scattering Signatures of Kitaev Spin Liquids in  $\text{A}_2\text{IrO}_3$  Iridates with  $\text{A}=\text{Na}$  or  $\text{Li}$ , *Phys. Rev. Lett.* **113**, 187201 (2014).
- [4] J. Knolle, D. L. Kovrizhin, J. T. Chalker and R. Moessner, Dynamics of a Two-Dimensional Quantum Spin Liquid: Signatures



- of Emergent Majorana Fermions and Fluxes, *Phys. Rev. Lett.* **112**, 207203 (2014).
- [5] J. Nasu, J. Knolle, D. L. Kovrizhin, Y. Motome and R. Moessner, Fermionic response from fractionalization in an insulating two-dimensional magnet, *Nat. Phys.* **12**, 912 (2016).
- [6] J. Yoshitake, J. Nasu and Y. Motome, Fractional Spin Fluctuations as a Precursor of Quantum Spin Liquids: Majorana Dynamical Mean-Field Study for the Kitaev Model, *Phys. Rev. Lett.* **117**, 157203 (2016).
- [7] A. Glamazda, P. Lemmens, S.-H. Do, Y. S. Choi, and K.-Y. Choi, Raman spectroscopic signature of fractionalized excitations in the harmonic-honeycomb iridates  $\beta$ - and  $\gamma$ - $\text{Li}_2\text{IrO}_3$ , *Nat. Commun.* **7**, 12286 (2016).
- [8] Heung-Sik Kim, V. V. Shankar, Andrei Catuneanu, and Hae-Young Kee, Kitaev magnetism in honeycomb  $\text{RuCl}_3$  with intermediate spin-orbit coupling, *Phys. Rev. B* **91**, 241110 (2015).
- [9] K. W. Plumb, J. P. Clancy, L. J. Sandilands, V. V. Shankar, Y. F. Hu, K. S. Burch, H.-Y. Kee, and Y.-J. Kim,  $\alpha$ - $\text{RuCl}_3$ : A spin-orbit assisted Mott insulator on a honeycomb lattice, *Phys. Rev. B* **90**, 041112(R) (2014).
- [10] J. G. Rau, Eric Kin-Ho Lee, and Hae-Young Kee, Generic Spin Model for the Honeycomb Iridates beyond the Kitaev Limit, *Phys. Rev. Lett.* **112**, 077204 (2014).
- [11] S. M. Winter, Y. Li, H. O. Jeschke, and R. Valenti, Challenges in design of Kitaev materials: Magnetic interactions from competing energy scales, *Phys. Rev. B* **93**, 214431 (2016).
- [12] R. Yadav, N. A. Bogdanov, V. M. Katukuri, S. Nishimoto, J. van den Brink, and L. Hozoi, Kitaev exchange and field-induced quantum spin-liquid states in honeycomb  $\alpha$ - $\text{RuCl}_3$ , *Sci. Rep.* **6**, 37925 (2016).
- [13] S. H. Baek, S.-H. Do, K.-Y. Choi, Y. S. Kwon, A. U. B. Wolter, S. Nishimoto, Jeroen van den Brink, and B. Büchner, Evidence for a Field-Induced Quantum Spin Liquid in  $\alpha$ - $\text{RuCl}_3$ , *Phys. Rev. Lett.* **119**, 037201 (2017).
- [14] A. Banerjee, C. A. Bridges, J.-Q. Yan, A. A. Aczel, L. Li, M. B. Stone, G. E. Granroth, M. D. Lumsden, Y. Yiu, J. Knolle, S. Bhattacharjee, D. L. Kovrizhin, R. Moessner, D. A. Tennant, D. G. Mandrus, and S. E. Nagler, Proximate Kitaev quantum spin liquid behavior in a honeycomb magnet, *Nat. Mater.* **15**, 733 (2016).
- [15] S.-Y. Park, S.-H. Do, K.-Y. Choi, D. Jang, T.-H. Jang, J. Schefer, C.-M. Wu, J. S. Gardner, J. M. S. Park, J.-H. Park, and Sungdae Ji, Emergence of the Isotropic Kitaev Honeycomb Lattice with Two-dimensional Ising Universality in  $\alpha$ - $\text{RuCl}_3$ , [arXiv:1609.05690](https://arxiv.org/abs/1609.05690).
- [16] L. J. Sandilands, Y. Tian, K. W. Plumb, Y.-J. Kim, and K. S. Burch, Scattering Continuum and Possible Fractionalized Excitations in  $\alpha$ - $\text{RuCl}_3$ , *Phys. Rev. Lett.* **114**, 147201 (2015).
- [17] Zhe Wang, S. Reschke, D. Huvonen, S.-H. Do, K.-Y. Choi, M. Gensch, U. Nagel, T. Rößler, and A. Loidl, Magnetic Excitations and Continuum of a Possibly Field-Induced Quantum Spin Liquid in  $\alpha$ - $\text{RuCl}_3$ , *Phys. Rev. Lett.* **119**, 227202 (2017).
- [18] A. Banerjee, J. Yan, J. Knolle, C. A. Bridges, M. B. Stone, M. D. Lumsden, D. G. Mandrus, D. A. Tennant, R. Moessner, and S. E. Nagler, Neutron scattering in the proximate quantum spin liquid  $\alpha$ - $\text{RuCl}_3$ , *Science* **356**, 1055 (2017).
- [19] A. U. B. Wolter, L. T. Corredor, L. Janssen, K. Nenkov, S. Schönecker, S.-H. Do, K.-Y. Choi, R. Albrecht, J. Hunger, T. Doert, M. Vojta, and B. Büchner, *Phys. Rev. B* **96**, 041405(R) (2017).
- [20] Seung-Hwan Do, Sang-Youn Park, Junki Yoshitake, Joji Nasu, Yukitoshi Motome, Yong Seung Kwon, D. T. Adroja, D. J. Voneshen, Kyoo Kim, T.-H. Jang, J.-H. Park, Kwang-Yong Choi, and Sungdae Ji, Majorana fermions in the Kitaev quantum spin system  $\alpha$ - $\text{RuCl}_3$ , *Nat. Phys.* **13**, 1079 (2017).
- [21] A. Glamazda, P. Lemmens, S. H. Do, Y. S. Kwon, and K.-Y. Choi, Relation between Kitaev magnetism and structure in  $\alpha$ - $\text{RuCl}_3$ , *Phys. Rev. B* **95**, 174429 (2017).
- [22] S. Reschke, F. Mayr, Zhe Wang, Seung-Hwan Do, K.-Y. Choi, and A. Loidl, Electronic and phonon excitations in  $\alpha$ - $\text{RuCl}_3$ , *Phys. Rev. B* **96**, 165120 (2017).
- [23] I. A. Leahy, Christopher A. Pocs, Peter E. Siegfried, David Graf, S.-H. Do, Kwang-Yong Choi, B. Normand, and Minhyea Lee, Anomalous Thermal Conductivity and Magnetic Torque Response in the Honeycomb Magnet  $\alpha$ - $\text{RuCl}_3$ , *Phys. Rev. Lett.* **118**, 187203 (2017).
- [24] Zhe Wang, Jing Guo, F. F. Tafti, Anthony Hegg, Sudeshna Sen, Vladimir A. Sidorov, Le Wang, Shu Cai, Wei Yi, Yazhou Zhou, Honghong Wang, Shan Zhang, Ke Yang, Aiguo Li, Xiaodong Li, Yanchun Li, Jing Liu, Youguo Shi, Wei Ku, Qi Wu, Robert J. Cava, and Liling Sun, Pressure-induced melting of magnetic order and emergence of new quantum state in  $\alpha$ - $\text{RuCl}_3$ , *Phys. Rev. B* **97**, 245149 (2018).
- [25] G. Santhosh, V. Sreenath, Arul Lakshminarayanan, and Rajesh Narayanan, Localized zero-energy modes in the Kitaev model with vacancy disorder, *Phys. Rev. B* **85**, 054204 (2012).
- [26] A. J. Willans, J. T. Chalker, and R. Moessner, Disorder in a Quantum Spin Liquid: Flux Binding and Local Moment Formation, *Phys. Rev. Lett.* **104**, 237203 (2010).
- [27] A. J. Willans, J. T. Chalker, and R. Moessner, Site dilution in the Kitaev honeycomb model, *Phys. Rev. B* **84**, 115146 (2011).
- [28] E. C. Andrade and M. Vojta, Magnetism in spin models for depleted honeycomb-lattice iridates: Spin-glass order towards percolation, *Phys. Rev. B* **90**, 205112 (2014).
- [29] F. Trouselet, G. Khaliullin, and P. Horsch, Effects of spin vacancies on magnetic properties of the Kitaev-Heisenberg model, *Phys. Rev. B* **84**, 054409 (2011).
- [30] S. Manni, Y. Tokiwa, and P. Gegenwart, Effect of nonmagnetic dilution in the honeycomb-lattice iridates  $\text{Na}_2\text{IrO}_3$  and  $\text{Li}_2\text{IrO}_3$ , *Phys. Rev. B* **89**, 241102 (2014).
- [31] P. Lampen-Kelley, A. Banerjee, A. A. Aczel, H. B. Cao, M. B. Stone, C. A. Bridges, J.-Q. Yan, S. E. Nagler, and D. Mandrus, Destabilization of Magnetic Order in a Dilute Kitaev Spin Liquid Candidate, *Phys. Rev. Lett.* **119**, 237203 (2017).
- [32] H. B. Cao, A. Banerjee, J.-Q. Yan, C. A. Bridges, M. D. Lumsden, D. G. Mandrus, D. A. Tennant, B. C. Chakoumakos, and S. E. Nagler, Low-temperature crystal and magnetic structure of  $\alpha$ - $\text{RuCl}_3$ , *Phys. Rev. B* **93**, 134423 (2016).
- [33] T. Isono, T. Terashima, K. Miyagawa, K. Kanoda and S. Uji, Quantum criticality in an organic spin-liquid insulator  $\kappa$ -(BEDT-TTF) $_2\text{Cu}_2(\text{CN})_3$ , *Nat. Commun.* **7**, 13494 (2016).
- [34] Q. Si, S. Rabello, K. Ingersent, and J. L. Smith, Locally critical quantum phase transitions in strongly correlated metals, *Nature (London)* **413**, 804 (2001).
- [35] D. R. Noakes, A correlation length measured by zero-field muon spin relaxation in disordered magnets, *J. Phys.: Condens. Matter* **11**, 1589 (1999).
- [36] D. R. Noakes and G. M. Kalvius, Anomalous zero-field muon spin relaxation in highly disordered magnets, *Phys. Rev. B* **56**, 2352 (1997).

- [37] R. Dally, T. Hogan, A. Amato, H. Luetkens, C. Baines, J. Rodriguez-Rivera, M. J. Graf, and S. D. Wilson, Short-Range Correlations in the Magnetic Ground State of  $\text{Na}_4\text{Ir}_3\text{O}_8$ , *Phys. Rev. Lett.* **113**, 247601 (2014).
- [38] J. A. Hodges, P. Bonville, A. Forget, A. Yaouanc, P. Dalmas de Réotier, G. André, M. Rams, K. Królas, C. Ritter, P. C. M. Gubbens, C. T. Kaiser, P. J. C. King, and C. Baines, First-Order Transition in the Spin Dynamics of Geometrically Frustrated  $\text{Yb}_2\text{Ti}_2\text{O}_7$ , *Phys. Rev. Lett.* **88**, 077204 (2002).
- [39] D. E. MacLaughlin, P.-C. Ho, Lei Shu, O. O. Bernal, Songrui Zhao, A. A. Dooraghi, T. Yanagisawa, M. B. Maple, and R. H. Fukuda, Muon spin rotation and relaxation in  $\text{Pr}_{1-x}\text{Nd}_x\text{Os}_4\text{Sb}_{12}$ : Magnetic and superconducting ground states, *Phys. Rev. B* **89**, 144419 (2014).